

1 **Detection of clustered anomalies in single-voxel morphometry as a rapid automated method for**
2 **identifying intracranial aneurysms.**

3 Mark C Allenby¹⁺, Ee Shern Liang^{2,3}, James Harvey^{2,3}, Maria A Woodruff¹, Marita Prior³, Craig D
4 Winter^{2,4}, David Alonso-Caneiro⁵

5 ¹Queensland University of Technology (QUT), Biofabrication and Tissue Morphology Group, Centre
6 for Biomedical Technologies, Institute of Health and Biomedical Innovation, Kelvin Grove, Qld 4059,
7 Australia

8 ²University of Queensland (UQ), Centre for Clinical Research, Faculty of Medicine, Herston, Qld 4006,
9 Australia

10 ³Department of Medical Imaging, Royal Brisbane & Women's Hospital, Herston, Qld 4029, Australia

11 ⁴Kenneth G Jamieson Department of Neurosurgery, Royal Brisbane & Women's Hospital, Herston, Qld
12 4029, Australia

13 ⁵Queensland University of Technology (QUT), Contact Lens and Visual Optics Laboratory, Centre for
14 Vision and Eye Research, School of Optometry and Vision Science, Kelvin Grove, Qld 4059, Australia

15 ⁺Corresponding author: mark.allenby@qut.edu.au

16

17 **Keywords:** Cerebral angiography; Intracranial aneurysm; Computational anatomy; Statistical shape
18 analysis

19 Highlights

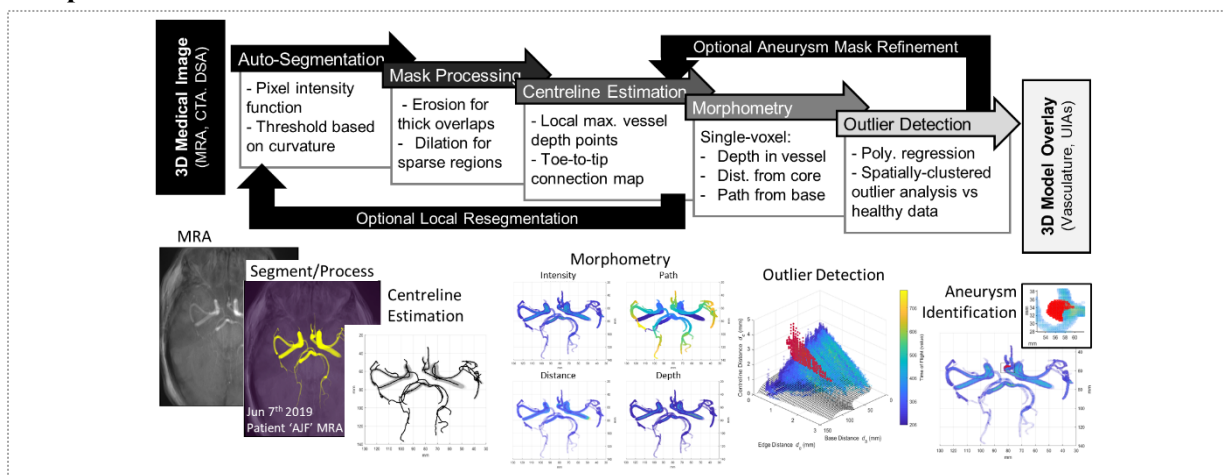
- 20 • Rapid and automated detection of unruptured intracranial aneurysms (UIAs) in MRAs
- 21 • Highly specific, sensitive UIA detection to reduce radiologist input for screening
- 22 • Detection is versatile to image resolution, modality and has tuneable mm sensitivity

23 Abstract

24 Unruptured intracranial aneurysms (UIAs) are prevalent neurovascular anomalies which, in rare
25 circumstances, rupture to create a catastrophic subarachnoid haemorrhage. Although surgical
26 management can reduce rupture risk, the majority of IAs exist undiscovered until rupture. Current
27 computer-aided UIA diagnoses sensitively detect and measure UIAs within cranial angiograms, but
28 remain limited to low specificities whose output requires considerable neuroradiologist interpretation
29 not amenable to broad screening efforts. To address these limitations, we propose an analysis which
30 interprets single-voxel morphometry of segmented neurovasculature to identify UIAs. Once
31 neurovascular anatomy of a specified resolution is segmented, interrelationships between voxel-specific
32 morphometries are estimated and spatially-clustered outliers are identified as UIA candidates. Our
33 automated solution detects UIAs within magnetic resonance angiograms (MRA) at unmatched 86%
34 specificity and 81% sensitivity using 3 minutes on a conventional laptop. Our approach does not rely
35 on interpatient comparisons or training datasets which could be difficult to amass and process for rare
36 incidentally discovered UIAs within large MRA files, and in doing so, is versatile to user-defined
37 segmentation quality, to detection sensitivity, and across a range of imaging resolutions and modalities.
38 We propose this method as a unique tool to aid UIA screening, characterisation of abnormal vasculature
39 in at-risk patients, morphometry-based rupture risk prediction, and identification of other vascular
40 abnormalities.

41 Graphical Abstract

42



43 1. Introduction

44 Intracranial aneurysms (IAs) are bulging, weak outpouchings of arteries that supply blood in the brain.
45 IAs are relatively common (2% to 5% prevalence; Figure 1A,B) but rarely discovered prior to incident
46 (International Study of Unruptured Intracranial Aneurysms (ISUIA), 2003). While most unruptured IAs
47 (UIAs) are asymptomatic, between 0.25% and 1% spontaneously rupture resulting in a subarachnoid
48 haemorrhage, a catastrophic event associated with a 40 to 50% mortality rate and with 50% of survivors
49 left with permanent disabilities (Figure 1C) (Leng et al., 2018; Thompson et al., 2015; van Gijn et al.,
50 2007; Williams and Brown, 2013). Therefore, early detection of UIAs is paramount so that management
51 to prevent future rupture can be considered (Figure 1D,E) (Mayo Foundation, 2017).

52
53 Aneurysms are detected and measured by radiologists interpreting computed tomography angiograms
54 (CTA), digital subtraction angiograms (DSA), or magnetic resonance angiograms (MRA) (Li et al.,
55 2009; Okahara et al., 2002). In 65% to 91% of cases UIA detection is incidental, and the frequency of
56 incidental detection has been rising due to an increased use of high-resolution intracranial MRAs which
57 do not require intravenous contrast or x-ray radiation (Corfield et al., 2010; Duan et al., 2018; Mair,
58 2015; Thompson et al., 2015). However, incidental detection is often by radiologists not specialised in
59 neuroanatomy who are not searching for an UIA. Therefore, detection sensitivity may be limited by the
60 shortage of experienced neuroradiologists able to review the increasing number of cranial radiology
61 examinations (Z. Shi et al., 2020).

62
63 Computational analyses can provide a rapid and automated identification of UIAs to serve as a
64 supportive reference to the nonspecialist radiologist for increased UIA detection accuracy. As
65 radiologist UIA detection sensitivity can be as low as 64% (Miki et al., 2016), computer-aided diagnoses
66 are attractive to improve accuracy while increasing the number of patient images analysed.
67 Conventional computer aided diagnoses detect UIAs using predetermined morphometries of interest
68 (curvature, sphericity, convexity), but have been less able to accurately identify irregular or small UIAs
69 (Jin et al., 2016; Yang et al., 2011). Recent machine learning approaches surmount conventional
70 limitations by detecting nonintuitive patterns consistent in aneurysmal regions, however their
71 performance must be conditioned on large annotated training sets often unavailable for rare incidentally
72 discovered UIAs. To date, conventional and machine learning approaches have achieved above 80%
73 sensitivity but at the cost of low specificity, generating 4 to 41 additional false positive UIAs per image
74 (Faron et al., 2019; Jin et al., 2016; Nakao et al., 2018; Stember et al., 2019; Ueda et al., 2019), which
75 may not reduce the time required during radiologist interpretation (Z. Shi et al., 2020).

76

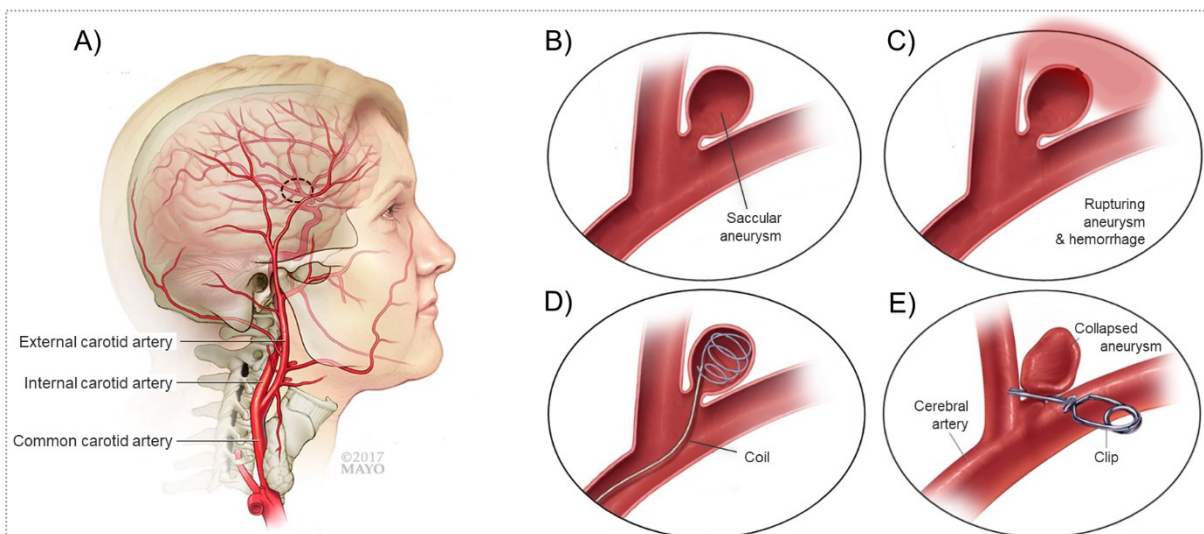


Figure 1: Intracranial aneurysm pathology and treatment. (A,B) IAs are bulging vessels within the head that are at risk of (C) rupture, causing subarachnoid haemorrhaging. Incidentally discovered UIAs can be monitored or surgically treated through (D) endovascular coiling or (E) neurosurgical clipping, which both carry nontrivial risk. *Adapted from the Mayo Foundation.*

77 Herein, we present an image analysis method based on a single-voxel morphometry approach to rapidly,
78 automatically, and specifically identify UIAs. Our algorithm automatically reconstructs 3D
79 presentations of patient neurovasculature from MRA, CTA, or DSA image datasets, then seeks to
80 identify UIA candidates based on three voxel morphometry attributes: distance from vessel centreline,
81 distance from vessel edge, and distance from image base. Identified UIA location and size are measured
82 and validated against clinician measurement. We analysed a cohort of 29 TOF MRAs presenting UIAs
83 who are benchmarked against 705 healthy TOF MRAs. Our automated algorithm is unique in its rapid
84 analysis of large 3D datasets without the need for training data or interpatient comparisons, its high and
85 tuneable specificity and sensitivity to identify fine features for clinical observation, and its versatility
86 in analysing a range of MRA resolutions as well as CTA and DSA modalities.

87

88 2. Methods and Calculation

89 Medical imaging records of 14 patients exhibiting at least one unruptured intracranial aneurysm and 27
90 healthy patients were retrospectively recruited from 2009 to 2019 and de-identified by the Medical
91 Imaging and Neurosurgery Departments of the Royal Brisbane & Women's Hospital according to
92 ethical clearances (LNR/2019/QRBW/49363). While each healthy patient was imaged once, many
93 patients harbouring UIAs were monitored over several years so that a total of 29 aneurysm-containing
94 TOF MRAs were imaged. The UIA parent vessel, location, and dimensions were described within
95 radiology reports and annotated within 2D slices of the image as illustrated in Figure S1. A further 678
96 healthy TOF MRAs were acquired from publicly available repositories (MIDAS and IXI) as described
97 previously (Mouches and Forkert, 2019). TOF MRA, CTA, and DSA images were captured in the
98 transverse direction at slice XY-resolutions spanning [0.18 x 0.18] to [0.61 x 0.61] mm/pixel and slice
99 steps with Z-resolutions from 0.38 to 2 mm/pixel.

100

101 A Dell Latitude 5300 laptop with 16 GB RAM and 1.90 GHz Intel Core i7-8665U processor produced
102 all timed runs. The proposed MATLAB algorithm (The MathWorks Inc, Natick, USA) resembles a
103 pipeline with several distinct steps, as illustrated in Figure 2 and detailed in the following subsections.

104

105 2.1. Global segmentation of a neurovascular mask (*Auto-Segmentation*)

106 Initially a universal threshold value was calculated to segment intravascular blood from surrounding
107 cranial tissue (Figure 3A). All voxel intensities throughout the CTA, DSA, or TOF-MRA image were
108 linearly divided into $n_{bin} = 50$ bins from maximal to minimal voxel intensity, similar to Nyúl et al.,
109 2000. Voxel intensity brightness, x , belonging to different tissue types, such as dim extravascular soft
110 tissue *versus* bone *versus* bright intravascular blood, was estimated by a sum of lognormal distributions
111 (Figure 3B) as previously performed for MRA images (Forkert et al., 2012):

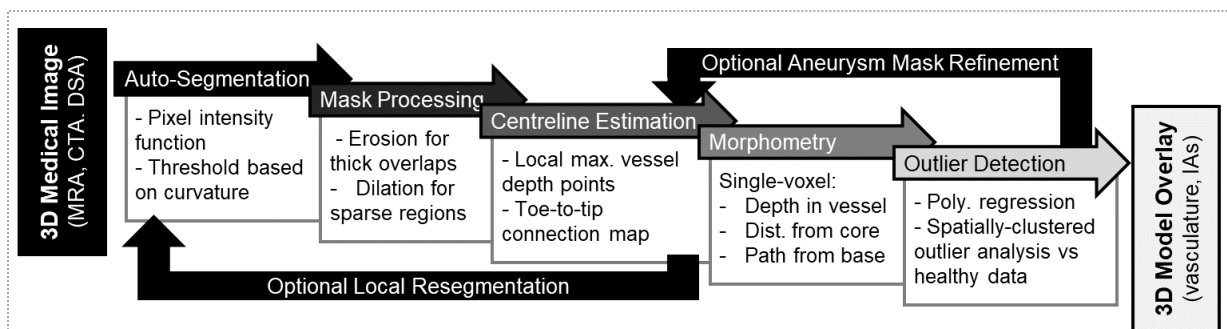


Figure 2: Intracranial aneurysm identification algorithm pipeline. The algorithm can input several different image modalities, including MRA, CTA, DSA. The images first undergo a global **Auto-Segmentation** to generate 2-3 tissue masks, the segmented neurovascular mask undergoes several **Mask Processing** steps, followed by a **Centreline Estimation** throughout the mask. Using the centreline, several **Morphometry** metrics are applied to measure geometrical properties of each voxel within the segmented vascular mask. The final **Outlier Detection** step identifies voxel properties consistent with normal vasculature, and regions which have large numbers of abnormal voxel properties. These regions are segmented as aneurysmal candidates for clinician assessment and computational measurement.

112
$$f_i(x; c_i, \mu_i, \sigma_i) = \frac{c_i}{x\sigma_i\sqrt{2\pi}} \exp\left(-\frac{(\log(x) - \mu_i)^2}{2\sigma_i^2}\right)$$

113 With tissue content scalar c_i and tissue intensity mean μ_i and standard deviation σ_i . Voxel intensities
 114 throughout the image were estimated as the sum of these lognormal distributions. In CTA images all 3
 115 aforementioned tissue types could be detected simultaneously, f_{1+2+3} , while in TOF MRA and DSA
 116 images only intravascular and extravascular tissue could be distinguished, f_{1+2} . The six or nine
 117 parameters of f_{1+2} or f_{1+2+3} were fit by minimising normalised error to the log voxel intensity of
 118 histogram bin 3 to 48 as to avoid overexposed and underexposed inconsistencies (removing $E_{bin} = 4\%$
 119 of bins from either end). A threshold value, T_v , was calculated to segment vessels from the brain tissue:

120
$$T_v = x \left[\frac{\partial^3 f_{(v-1)+v}}{\partial x^3} = 0 \right] + \left(\text{mode}(f_v) - x \left[\frac{\partial^3 f_{(v-1)+v}}{\partial x^3} = 0 \right] \right) \left(\frac{f_v(\text{mode}(f_v))}{f_{(v-1)+v}(\text{mode}(f_{(v-1)}))} \right)^{k_T}$$

121 Where v is the vessel mask index ($v = 2$ for TOF MRAs and DSAs, $v = 3$ for CTAs), where $\text{mode}(f_v) =$
 122 $\exp(\mu_v - \sigma_v^2)$ represents the mode of lognormal distribution f_v , and where $x \left[\frac{\partial^3 f_{(v-1)+v}}{\partial x^3} = 0 \right]$ describes
 123 a critical point of inflection change between the modes of f_v and f_{v-1} as shown in Figure 3B. Explicitly
 124 determined weight parameter k_T dictates neurovascular mask size, later leveraged to normalise
 125 segmentation across different MRA resolutions.

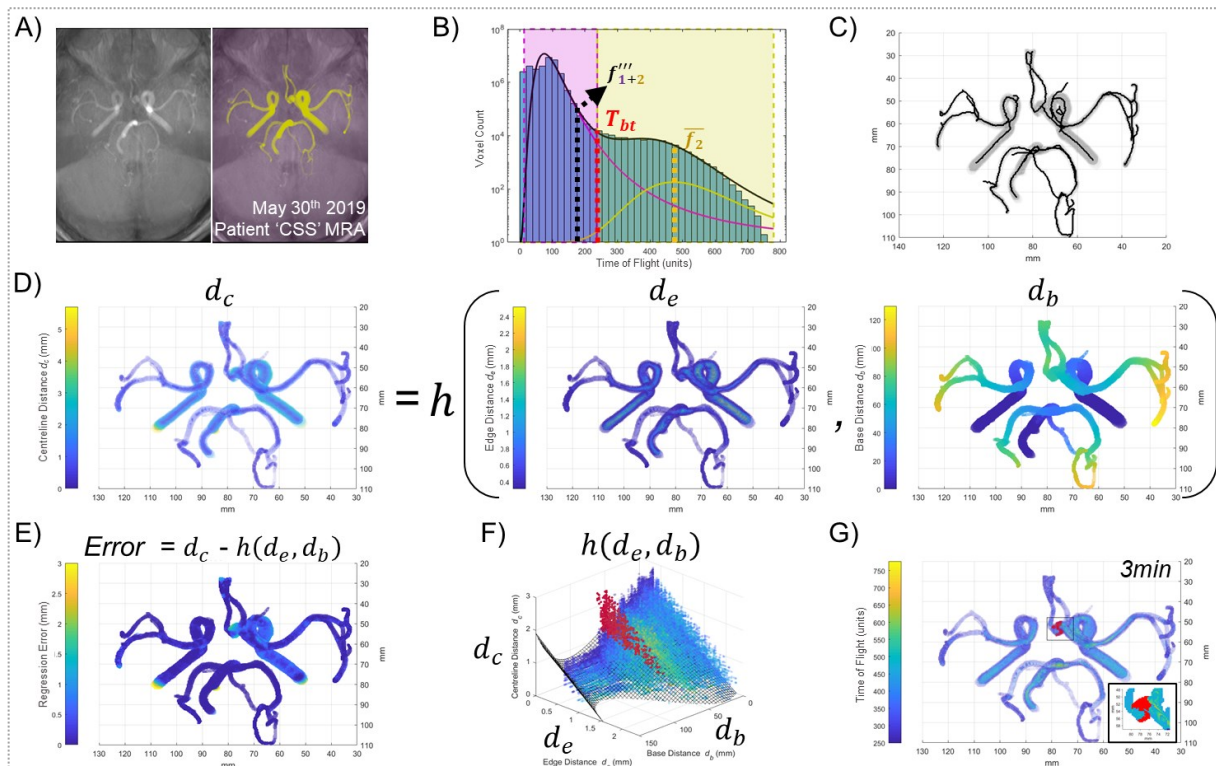


Figure 3: Intracranial segmentation, vascular network analysis, and aneurysm identification. (A,B) Segmentation of a 3D neurovascular mask based on a sum of lognormal distributions. (C) Identification of centrepoints via mask erosion, connecting adjacent centrepoints bottom-to-top into a network of branches, and measuring branch lengths and bifurcation points to detect centrepth length. (D) A voxel-specific polynomial regression was individually fit to measure the correlation between voxel distance from centreline (radius) versus voxel distance from vessel edge (depth) and voxel distance from base (path) for each image. (E) The error of actual voxel radius from expected voxel radius was measured and (F) outliers which were spatially-clustered together were identified as aneurysmal candidates, (G) overlaid in red over segmented mask image intensities with UIA region inset. The algorithm required 3 minutes to execute.

2.2. Evaluating single-voxel morphology (*Mask Processing and Centreline Estimation*)

Once the neurovascular mask is segmented, centrepoints are defined *via* a 3D medial surface thinning operation after filling closed voxel holes in the image. These centrepoints were then dilated and annealed together using a $m_{dil} = 2$ voxel rolling ball, and then centrepoints were re-identified in order to remove overestimated and overlapping small vessels using a range of binary morphological operations. A centreline was then connected through neighbouring centrepoints starting with the centrepoint in the lowest (most caudal) axial plane. When the next nearest unallocated centrepoint was further than $d_{link} = 1\text{mm}$ away, the terminal end of that vessel branch had been reached and the centreline for a new vessel was evaluated from the next lowest centrepoint. Branch endpoints between $d_{link} = 1\text{mm}$ and $d_{latch} = 2\text{mm}$ away from a previously allocated centrepoint were then connected to form the full neurovascular tree. Once completed, an interconnected branch network of centrelines through the segmented neurovascular mask was formed (Figure 3C).

Voxels within the vascular mask were evaluated using a range of morphometric properties: taking the vascular voxel as reference, d_c indicates the distance to vessel centreline, d_e distance to edge, and d_b distance to the carotid vessel, defined as the nearest terminal centrepoint at the bottom of the mask (Figure 3D). The first two properties were calculated using Euclidean distance operations performed on Boolean matrices between the neurovascular model and points defining the vessel centrelines. The third distance operation required sorting individual vessel branches' distance to the bottom of the vascular tree. Since many vessel branches intersect with many other vessel branches at multiple points, a combinatorial approach identified the tree branch path network which minimised total mask d_b across all intersecting branch entrances and exits.

2.3. Identifying aneurysms as outlier voxel clusters (*Morphometry and Outlier Detection*)

Each voxel's three morphometries formed a consistent relationship. That is, the distance of a voxel from the vessel centreline (d_c) depended on how far it was from the vessel edge (d_e) as well as its distance away from the base of the mask (d_b) (Figure 3E). A voxel far from the vessel centreline was more likely to be near the vessel edge and these distances were larger nearer the thick carotid arteries and not thin terminal cranial vessels. This relationship was characterised through fitting a polynomial regression through all voxels within the neurovascular masks ($>10,000$ voxels). For speed, a polynomial regression was used to estimate a voxel's centreline distance (d_c) which was first-order in its edge distance (d_e) and fourth-order in its base distance (d_b). Several other global and local polynomial regressions (loess) were compared but either exhibited a worse regression fit or prohibitively long processing times, respectively. Clusters of voxels which had centreline distances inaccurately predicted by our $h(d_e, d_b)$ regression were treated as outliers and considered to belong to either noncylindrical or inadequately large vessel anatomies, suggestive of vascular regions that may be aneurysm candidates (Figure 3F,E). Since this outlier detection is based on a single patient image and not a large dataset of patients, it can be particularly universal to anatomical and imaging differences.

The definition of these voxel cluster outliers, or aneurysm candidates, can be tailored for high or low detection sensitivity based on user demand and clinical application. For our multi-repository validation we identified aneurysm candidates as voxel clusters beyond the polynomial regression's $E_{out} = 96\%$ confidence interval and larger than $V_{min} = 17.3h(d_e, d_b) + 1.5 \text{ mm}^3$ to allow for aneurysm detection in large central as well as small peripheral vessels. Voxel centreline distance estimated from $h(d_e, d_b)$ typically varied from 1.5 mm at the carotid artery base to 0 mm at the terminal ends of peripheral arteries. We later demonstrate how users can decrease E_{out} and V_{min} to increase detection sensitivity for small or emergent aneurysmal buds.

2.4. Refining poorly-segmented neurovascular masks (*Optional Local Resegmentation*)

For poor quality images with under- or over-saturated cranial images, it may be difficult to analyse morphometry due to a fusing of adjacent vessels or an inaccurate capture of the aneurysm shape (Figure 4A). In such cases, a more accurate segmentation can be achieved through re-estimating the segmentation threshold for many small regions throughout the vessel structure. However, this more accurate local segmentation comes at the price of increased time and experimentally evaluated

180 parameters. This local segmentation procedure proceeds by evaluating the vessel centrepnts produced
 181 from Section 2.2 and drawing spherical neighbourhoods around these centrepnts for re-segmentation.
 182 Next, successive centrepnts neighbourhood are considered until all their contained vessel masks have
 183 been re-segmented. Finally, the remaining image space is also re-segmented based on the threshold
 184 assigned to each voxel's closest neighbourhood, which allows for significant mask growth.

185

186 The diameter of these spherical neighbourhoods must be large enough to consider the thickest vessel
 187 diameter while sampling frequency along the centrepnts must be fine enough to not allow
 188 unconsidered gaps. To ensure adequate neighbourhood overlap, sampling frequency was dictated by
 189 spherical neighbourhood centring spaced to sphere and vessel radius:

190

$$d_{max} = k_d \sqrt{4R_n^2 - R_v^2}$$

191 Where R_n is the desired spherical neighbourhood radius, R_v is the calculated vessel mask radius, and
 192 k_d is a user-defined scalar between 0 and 1 adjusting neighbourhood overlap, where $k_d = 1$ would
 193 allow neighbourhoods to overlap just enough to encompass the current vessel radius. Spherical
 194 neighbourhoods which are too large or too infrequent would limit the effectiveness of the local

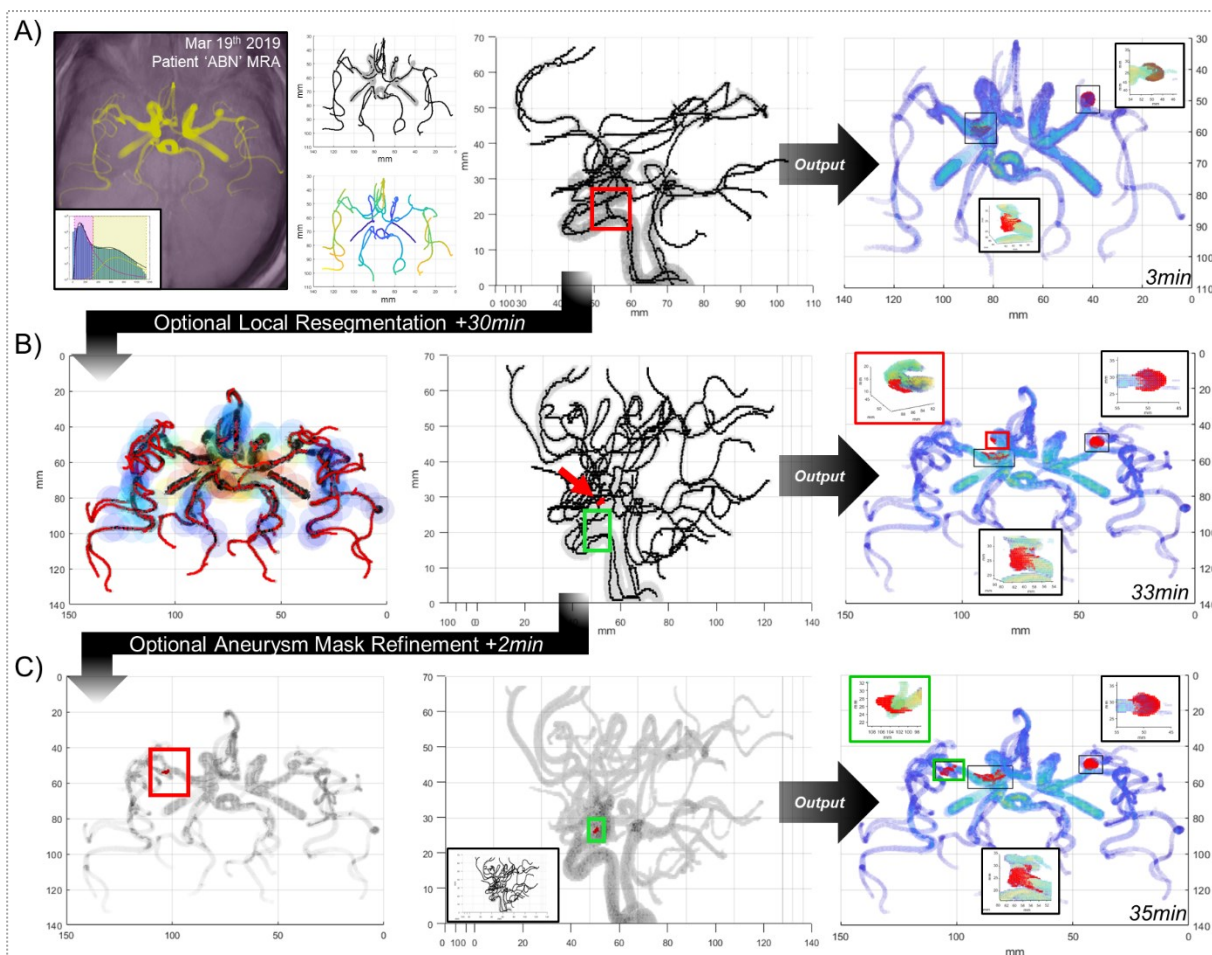


Figure 4: Optional refinements of the UIA identification pipeline. (A) While the algorithm pipeline presented in Figures 2 and 3 is rapid, sensitive, and specific, it struggles with large convoluted neurovascular masks with overlapping vasculature. When a more detailed mask and IA identification is required at the expense of increased computational time, additional pipeline refinements can be performed. (B) A local resegmentation can be performed which recalculates the threshold of the neurovascular mask within spherical neighborhoods along the previous centerlines, and then expands those thresholds into the remainder of the image. This resegmentation serves to cull vessel thicknesses within overlapping high-signal regions and enhance the vessel mask into regions with low signal and can be iterated as desired. (C) A mask refinement can be performed which surveys an aneurysmal candidate and deletes vessel centerlines which enter an aneurysm to provide a more complete IA segmentation.

195 segmentation, but small or frequent neighbourhoods create unnecessary computational burden. Our
196 masks appeared to work best with $R_n = 2.75$ mm and $k_d = 0.5$ to allow for re-segmented masks to
197 grow in dim peripheral regions but also shrink in bright carotid regions (Figure 4B).

198
199 Spherical neighbourhoods can predominately be comprised of brain tissue near shrinkingly small
200 vessels, resulting in only one lognormal distribution of low voxel intensities and skewing the calculation
201 of a threshold value to extremely low values for re-segmentation, causing brain tissue to be interpreted
202 as vessels. To avoid this, we ensure these neighbourhood minimum or maximum thresholds do not
203 exceed predefined global limits. Specifically, we propose: if $T_v < T_{min}$, then $T_v = T_{min} =$
204 $x \left[\frac{\partial^2 f_{1+2}}{\partial x^2} = 0 \right]$ or if $T_v > T_{max}$, then $T_v = T_{max} = \text{mode}(f_2)$, which represent the minimum and
205 maximum values T_v is defined to have if two or more tissues are present.

206

207 **2.5. Refining poorly-segmented aneurysmal masks (Optional Aneurysm Mask Refinement)**

208 For several neurovascular masks harbouring an intracranial aneurysm, a network of vessel centrepnts
209 determined by the binary erosion technique outlined in Section 2.2 could erroneously include
210 centrepnts of the UIA leading to misidentification or an incomplete aneurysmal mask. To address this
211 issue, we added a function which first identifies UIA candidates with increased sensitivity ($E_{out, re} =$
212 60%) as in Section 2.3, then for each UIA candidate determines whether a nearby branch of centrepnts
213 terminates. Branches closer than R_{cull} from the UIA centroid and within d_{cull} from terminal centrepnt
214 are culled. This process can be applied to trim many small branches diverging from major vessels by
215 lowering other IA detection parameters such as V_{min} from Section 2.3. After the UIA-entering branches
216 are deleted, the UIA detection is re-run at the original threshold sensitivity (Figure 4C).

217

218 **3. Results**

219 Our image analysis approach is conventional in specifying which morphometry attributes are indicative
220 of UIAs but also mimics machine learning approaches by identifying unique patterns in single-voxel
221 morphometries for each image. In doing so, our algorithm becomes adaptable to image quality and
222 detection accuracy inputs. Our image processing steps require user-selected parameters (Table 1) which
223 must be validated to be widely applicable but whose detection sensitivity can also be adjusted to detect
224 fine or coarse aneurysmal candidate regions. Correspondingly, we validate the accuracy and
225 demonstrate the versatility of our statistical approach herein.

226

227 **3.1. Rapid automated IA detection is sensitive and specific**

228 The sensitivity of this algorithm was validated over a cohort of patients presenting to the Royal Brisbane
229 and Women's Hospital (RBWH) between 2009 and 2019 who harboured an UIA imaged by TOF MRA
230 (14 patients, 29 TOF MRA images). Several patients were imaged on more than one occasion to monitor
231 aneurysmal shape changes over time and assess rupture risk for surgical decision-making. Accuracy of
232 algorithm-identified aneurysm location and size was validated by interventional radiologists asked to
233 retrospectively annotate, measure, and comment on unedited TOF MRA image slices while blinded to
234 the algorithm's detection as illustrated in Figure S1. The specificity of this algorithm was validated over
235 a cohort of 27 patients not identified to have an intracranial aneurysm using TOF MRA and DSA.
236 Additionally, the specificity of this algorithm was further validated over public IXI and MIDAS
237 repositories for another 678 healthy TOF MRA patients (Mouches and Forkert, 2019). Images were
238 automatically excluded from consideration if severe TOF MRA imaging artefacts interrupted the
239 neurovascular mask construction ($N = 6$), or if only 1 lognormal distribution could be detected during
240 segmentation ($N = 94$ to $N = 154$ depending on normalisation) so that a neurovascular mask could not
241 be identified. This exclusion criteria and rate is consistent with prior publications (14% to 23% excluded
242 versus 20% previously; Mouches and Forkert, 2019).

243

244 To provide a fair comparison, all validations were performed with identical parameters, which also
245 ensured the algorithm was fully automated. The speed of the algorithm varied between 1.5 and 12 min
246 primarily depending on image resolution (which affected image matrix size), and neurovascular mask
247 volume (which affected time-intensive binary distance operations). The 734 TOF MRAs varied across

Table 1: Summary of algorithm parameters. These algorithm parameters are grouped into the pipeline steps specified in Figure 2 and throughout methodology Section 2. Values are provided as a guide to replicate the algorithm performance in this paper but can be changed based on user preferences. Detection sensitivity was lowered in Figure 7 to demonstrate the impact of varied detection sensitivity.

Section	Symbol	Notes	Range	Value	Units
Model segmentation (Section 2.1)	n_{bin}	Histogram bin number	\mathbb{Z}^+	50	-
	E_{bin}	Excluded peripheral bins	\mathbb{R}^+	4	%
	k_T	Segmentation threshold parameter	\mathbb{R}^+	$0.3134R_{XY}^{-1.522}$	-
Mask processing & centreline estimation (Section 2.2)	D_{dil}	Length to dilate and erode mask	\mathbb{R}^+	0.7	mm
	d_{link}	Max distance between centre-points of the same vessel branch	\mathbb{R}^+	1	mm
	d_{latch}	Max distance to connect two vessel branches	\mathbb{R}^+	2	mm
Morphometry & outlier analysis (Section 2.3)	E_{out}	Error threshold to identify outliers	\mathbb{R}^+ [0–100]	96	%
	V_{min}	Size threshold to identify outliers	\mathbb{Z}^+	$17.3h(d_e, d_b) + 1.5$	mm ³
Optional: local resegmentation (Section 2.4)	R_n	Spherical diameter around centre-point to re-threshold	\mathbb{Z}^+	2.75	mm
	k_d	Overlap ratio between spherical neighbourhoods	\mathbb{R}^+ [0–1]	0.5	-
Optional: IA refinement (Section 2.5)	$E_{out, re}$	Pre-threshold for potential outliers	\mathbb{R}^+ [0–100]	60	%
	R_{cull}	Culled branch candidate distance from UIA	\mathbb{R}^+	10	mm
	d_{cull}	Tip-to-bifurcation length of small isolated branch to cull	\mathbb{R}^+	6.6	mm

248 10 image resolutions from 0.26 to 0.80 mm/voxel (Figure S2). Median processing times per TOF MRA
 249 image were 5.2 min, 2.7 min, and 2.0 min for RBWH, MIDAS, and IXI datasets respectively.

250
 251 There was a clear trend between XY image resolution and segmented mask volume and length. This
 252 trend led to the under-segmentation of low-resolution TOF MRA images within the IXI and MIDAS
 253 repository datasets creating large neurovascular masks containing additional peripheral vessels
 254 irrelevant for aneurysmal identification such as venous sinuses and torcula. An exponential relationship
 255 between XY image resolution and the k_T thresholding parameter was defined to normalise segmentation
 256 across resolutions (Figure 5, Figure S2). Without normalisation, images from MIDAS and IXI
 257 repositories were significantly different to RBWH with respect to mask length and volume. After
 258 normalisation, mask lengths were more equal between repositories.

259
 260 The algorithm's identification achieved 81% sensitivity and 86% specificity, correctly identifying UIAs
 261 within 17 of 21 TOF MRAs within the RBWH database, and correctly identifying no aneurysms within
 262 518 of 602 normal patient images within RBWH, IXI, and MIDAS databases (Figure 5). Nearly 80%
 263 of the 84 false positive UIA locations existed within the carotid siphon, where several tortuous bends
 264 deviate from normal cylindrical vessel geometry and poor contrast or segmentation could appear as
 265 though the siphon self-intersects (Bogunović et al., 2012; Duan et al., 2019). Most other false positive
 266 UIAs appeared within small overlapping peripheral arteries, especially for low-resolution images, such
 267 as the M3 and M4 segments in the anterior cerebral artery (as illustrated in Figure S3).

268 269 **3.2. Detection pipeline is versatile to imaging resolution and MRA, CTA, or DSA modalities**

270 This algorithm was principally developed for TOF MRA imaging, which represents a promising
 271 technique to 3D image intracranial vasculature without the use of intravenous contrast or x-ray
 272 radiation. However, many patients are unable to be imaged via MRA, including those who have

273 previously had aneurysmal interventions with metallic neurosurgical clips or endovascular coils.
 274 Higher-resolution CTA and DSA are frequently employed as a primary or secondary imaging method
 275 to confirm aneurysm location and shape. In our RBWH MRA datasets, 82% of aneurysm-harboring
 276 patients also had CTA or DSA imaging performed.

277

278 This algorithm was applied to abnormal and normal CTA and DSA images in Figure 6. These 3D
 279 images frequently have much higher XY resolution (0.15 - 0.30 mm/voxel) but lower Z resolution (1.0
 280 - 2.0 mm/voxel) which can cause artefacts for vessels coarsely resolved in the Z-dimension. Even so,
 281 the algorithm was able to segment and identify UIAs within MRA, CTA, and DSA datasets, indicating
 282 its versatility across imaging modalities and clinical needs.

283

284 3.3. Adjustable detection sensitivity can identify early budding aneurysms

285 The algorithm can be tailored to suit specific clinical needs by adjusting two sensitivity parameters: the
 286 error threshold (E_{out}) and the size threshold (V_{min}) which identify outliers as candidate aneurysm
 287 regions. During algorithm validation and in Figure 5, these sensitivity parameters were kept constant
 288 across the 3 patient datasets and more than 700 patient images. However, sensitivity can be improved

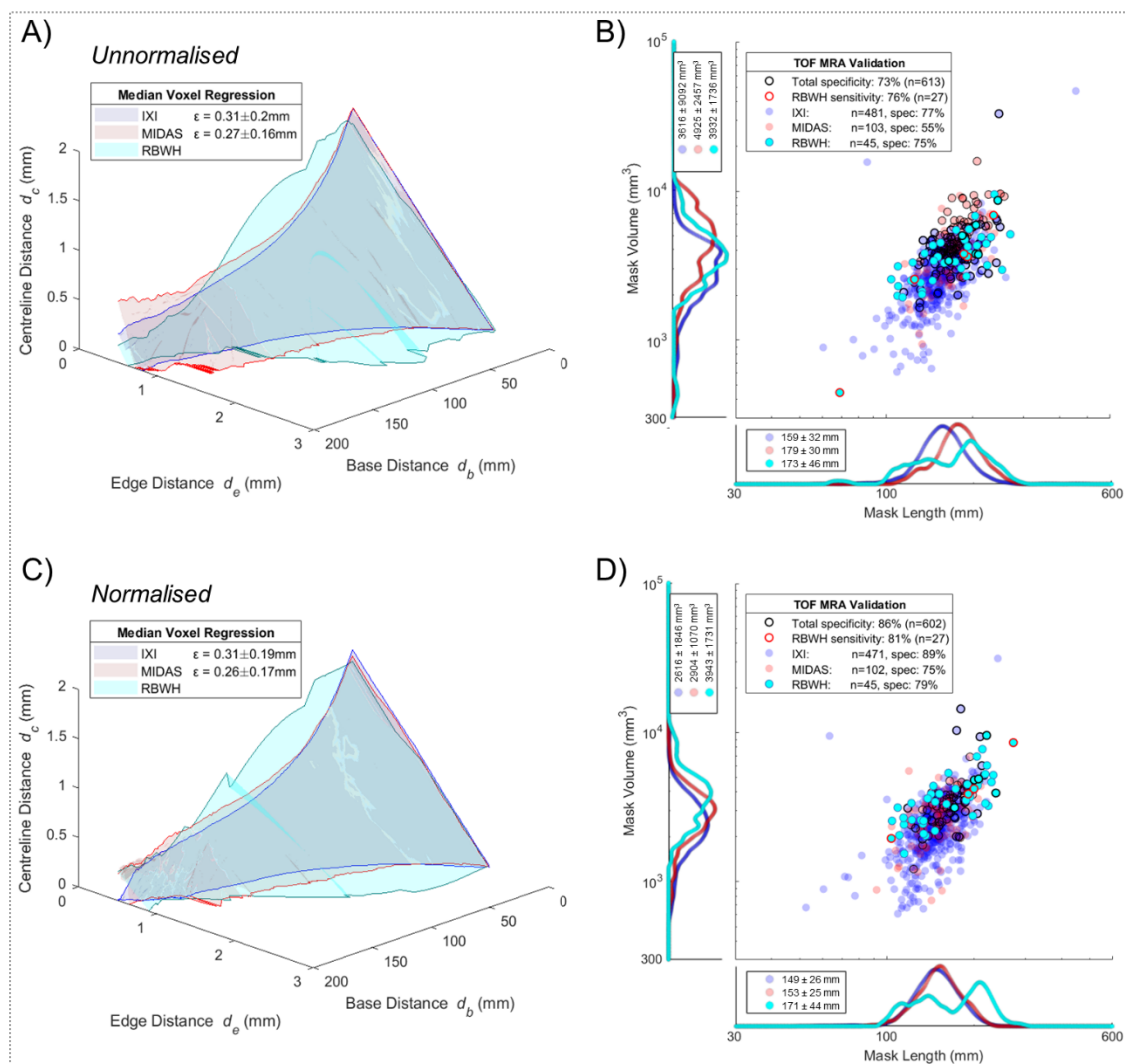


Figure 5: Algorithm validation and normalisation. (A,C) Median $h(d_e, d_b)$ regressions of single-voxel morphometry for IXI ($N = 571$), MIDAS ($N = 107$) and RBWH ($N = 45$) repositories, where spatially-clustered voxels beyond a 96% confidence interval from individual regressions were considered UIA candidates. (B,D) Specificity and sensitivity were evaluated with false-positives circled black and false-negatives circled red, where errors existed predominately in large and long neurovascular masks. A trend between low resolution MRAs producing large segmented masks was normalised from (A,B) $k_T = 1.78$ by applying (C,D) $k_T = 0.3134 \cdot R_{XY}^{-1.522}$, as detailed in Figure S2.

289 at the cost of specificity (false-positive aneurysm detection) by decreasing the minimum error or cluster
 290 size of candidate aneurysm regions to highlight small or slightly bulging intracranial vessels. While
 291 these bulging regions may be false positives generated by atypically tortuous neurovasculature or
 292 imaging or segmentation artefacts, lowering these detection thresholds could be useful to suggest
 293 potential small, difficult-to-spot, or secondary UIAs for radiological assessment.
 294

295 To demonstrate the utility of this algorithm's tuneable sensitivity, we identified a patient harbouring an
 296 UIA which was monitored over 5 TOF MRA imaging sessions between 2012 and 2018. During the
 297 initial visit in 2012, a large 4 x 3 mm saccular aneurysm was discovered on the left peripheral
 298 communicating artery and was monitored over the following 6 years. In 2018, a second bilateral
 299 aneurysm was discovered which led to a surgical decision of intervention. Using our algorithm at Figure
 300 5's validation sensitivity, we identified the same UIAs at the same timepoints as the clinicians identified.
 301 We then repeated our algorithm using a heightened sensitivity which detected abnormal voxel clusters

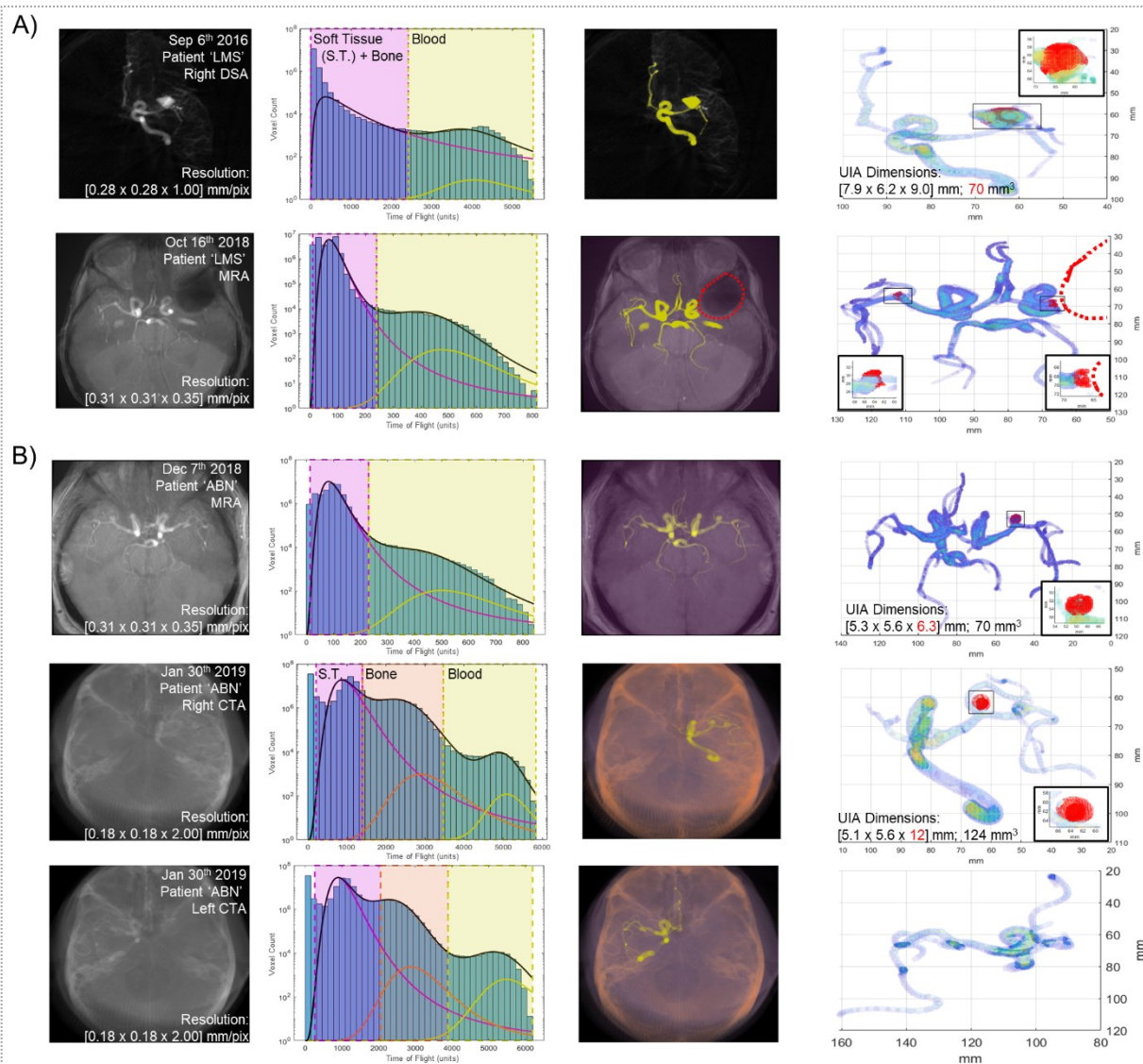


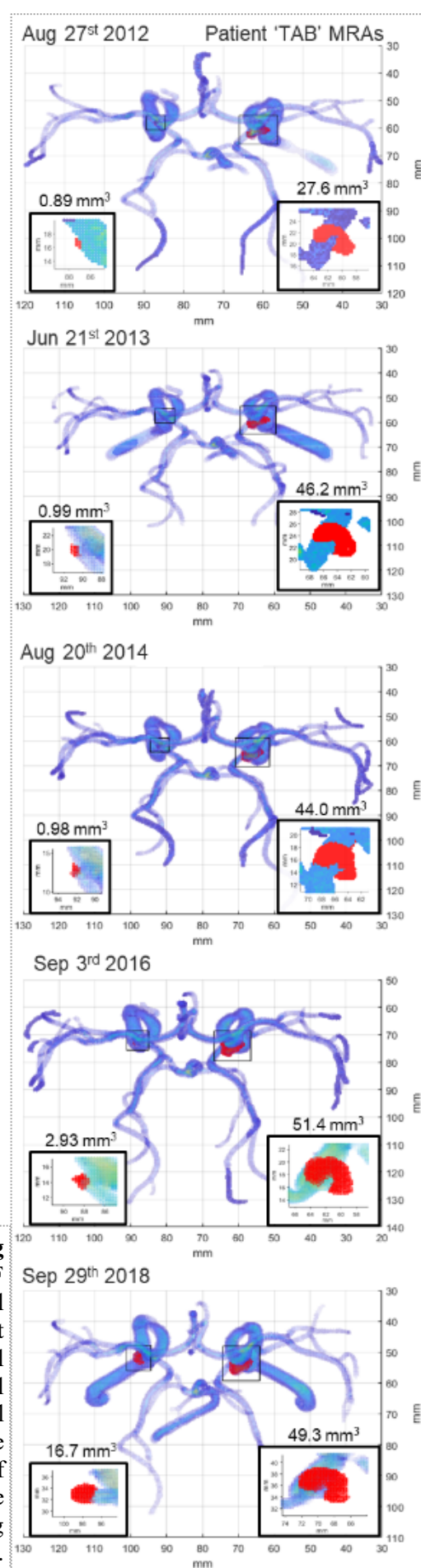
Figure 6: Algorithm versatility for different medical imaging modalities and resolutions. (A) Neurovasculature was imaged using right-hemisphere DSA (first row) before being rushed to surgery for endovascular coil placement. Later, this patient was imaged using TOF MRA with a large artefact at the location of the prior aneurysm (second row, red dotted circle). (B) Neurovasculature was imaged using TOF MRA or CTA for both brain hemispheres on the same date. Columns, from left to right, include original medical image mean intensity projection, voxel intensity histogram fit to the sum of 2 or 3 lognormal regressions, segmented soft tissue, bone, and/or vasculature masks, and mask voxel intensity heatmap with identified aneurysms. Measured UIA dimensions from CTA or DSA appear inaccurate, highlighted in red text. Abbreviation S.T. corresponds to 'soft tissue'.

302 larger than 0.7 mm^3 . Using this sensitivity, we could observe
303 the growth of a small bulging region ($0.9 - 2.9 \text{ mm}^3$) at the
304 same location that the bilateral aneurysm would form 6 years
305 earlier, with no other false-positives detected (Figure 7).
306 While such small regional voxel abnormalities may often
307 occur due to imaging artefact or normal variances within
308 neurovascular anatomy, such a sensitive identification could
309 identify regions of radiologic interest similar to those
310 performed in recent computer-aided diagnosis approaches
311 (Faron et al., 2019; Miki et al., 2016; Nakao et al., 2018;
312 Stember et al., 2019; Ueda et al., 2019).

313
314 Previous computer-aided diagnoses have reached high levels
315 of sensitivity but have done so exhibiting very low specificity,
316 incorrectly detecting several false-positive UIAs per image.
317 These approaches still require substantial radiological
318 interpretation to exclude these false-positives and may not
319 improve the number of medical images a radiologist can
320 assess within a certain amount of time. Furthermore, detection
321 rates vary between radiologists and neuroradiologists and our
322 approach enables an unbiased detection and characterisation
323 of UIAs at mm^3 resolution (Okahara et al., 2002). This user-
324 adjustable approach will better provide both high-specificity
325 screening of UIA presence and high-sensitivity UIA
326 characterisation toward reduced radiologist workloads.

327 4. Discussion

328 We propose a new method to identify UIAs within 3D medical
329 angiograms, principally within widely-used TOF MRAs
330 (Thompson et al., 2015). The key innovations of our method
331 include high sensitivity with high specificity and user-defined
332 versatility while utilising large 3D medical images
333 independent of interpatient comparison. Our method reaches
334 at least an 81% sensitivity and 86% specificity, on-par with
335 conventional computer aided MRA diagnoses achieving up to
336 83.6% sensitivity and 75% specificity, while analysing MRAs
337 10-fold faster (Miki et al., 2016; Štěpán-Buksakowska et al.,
338 2014; Yang et al., 2011). Sensitivities above 90% have been
339 reached with other machine learning approaches but only
340 while generating as many as 4 - 22 false-positives per image
341 indicating specificities near 0% (Faron et al., 2019; Nakao et
342 al., 2018; Shi et al., 2020; Stember et al., 2019; Ueda et al.,
343 2019). One recent approach identified UIAs inside small
344 $\sim 30\text{mm}$ vessel segments with 88.5% sensitivity and 98.5%



345 specificity, but required 8 hours to manually segment each neurovascular model into pieces (Yang et
346 al., 2020). These machine learning approaches rely on large training datasets which may be difficult to
347 acquire and time-consuming to train for 3D angiograms of incidentally-discovered UIAs. Altogether,
348 computer-aided diagnosis have only increased radiologist diagnosis sensitivity from 64% to 69% and
349 have not reduced radiologist interpretation time (Miki et al., 2016; Z. Shi et al., 2020; Štěpán-
350 Buksakowska et al., 2014).

351
352 Our clustered anomaly detection method presented in this paper calculates a unique morphometry
353 regression for each individual image, and is not reliant on a large dataset of training images typical of
354 current machine learning approaches (Faron et al., 2019; Miki et al., 2016; Štěpán-Buksakowska et al.,
355 2014; Yang et al., 2011). And while current approaches frequently analyse medical images of only one
356 single imaging modality and resolution, our method was evaluated over 10 different TOF MRA
357 resolutions from 5 different hospitals and also applied to several CTA and 3D DSA images. A specific
358 utility of our method is its ability to tailor mask segmentation and UIA detection sensitivity depending
359 on user demand. If high sensitivity at the cost of low specificity is preferred, the UIA detection threshold
360 can be lowered. This could also assist with the detection of secondary UIAs or abnormal budding
361 regions as demonstrated in Figure 7. While our method could mimic current approaches by determining
362 one average morphometry regression across our large healthy dataset of images, such a method would
363 be limited due to the anatomical complexity and variability common to intracranial angiograms. This
364 variability can be reduced through image normalisation approaches, but a recent neurovascular atlas
365 (544 healthy TOF MRAs) indicates MRA normalisation may only allow consistent segmentation for
366 major arteries (Mouches and Forkert, 2019). Our approach has several limitations. It relies on the
367 construction of an interconnected centreline throughout all vessels, which occasionally cannot be
368 achieved due to TOF MRA bleb artefacts (Corfield et al., 2010; Mair, 2015). Furthermore, TOF MRA
369 imaging achieves poorer resolution than CTA or DSA methodologies (Lin et al., 2018), limiting the
370 detection of small aneurysms in peripheral neurovasculature. Detection sensitivity increased with local
371 image resegmentation and would likely further increase with enhanced centreline estimation, image
372 normalisation, or local polynomial regression or smoothing algorithms (Kerrien et al., 2017; Pelka et
373 al., 2017; Wong and Chung, 2007). We prototyped several such developments which can improve
374 sensitivity or specificity slightly but require substantial increases in processing time. Finally, our large
375 TOF MRA dataset is heavily biased toward healthy patients. It will be necessary to recruit additional
376 patient cases harbouring rare incidentally discovered UIAs in order to have greater confidence in our
377 detection sensitivity.

378
379 The detection of UIAs prior to rupture allows for careful management to avoid haemorrhage.
380 Fortunately, the incidental discovery of UIAs is becoming more frequent due to the increased use and
381 resolution of MRA, a neurovascular imaging technique which does not require intravenous contrast or
382 x-ray radiation (Thompson et al., 2015). While MRA may be a promising angiography technique to
383 screen for UIAs in patients with a strong family history or those presenting migraines (Micieli and
384 Kingston, 2019), it would be laborious, expensive, and unfeasible to engage expert neuroradiologists to
385 review large numbers of cranial angiograms within a publicly-funded clinical imaging department (Z.
386 Shi et al., 2020). In addition, once a UIA is discovered the surgical decision-making process remains
387 ‘complex and controversial’ where as many as 58.3% of UIA patients undergo neuro or endovascular
388 surgery (International Study of Unruptured Intracranial Aneurysms (ISUIA), 2003). While rupture risk
389 is associated with UIA size and location aspect ratio, neck-to-body ratio, and intra-UIA fluid dynamics
390 and wall thickness (Duan et al., 2018; Ishibashi et al., 2009; Russell et al., 2013), no widely-accepted
391 prediction of rupture exists to guide surgical decision-making, and recent studies suggest decision-
392 making has favoured interventional methods. Automated and rapid computational analyses of cranial
393 angiograms could enable an unbiased screening of patient neurovasculature for UIAs and future
394 identification of morphometric or blood flow features correlating to future UIA size and shape changes,
395 surgical decisions, or rupture risk, or assessment of other vascular malformations (Chien et al., 2020;
396 Huang et al., 2013; Z. Shi et al., 2020).

397 5. Conclusion

398 We have developed a rapid and automated 3D cranial angiogram analysis algorithm which segments
399 neurovasculature, assesses single-voxel relationships between arterial morphometries, and identifies
400 spatially-clustered voxel outliers as a potential UIA candidate. This method represents a significant
401 improvement due to its high specificity and sensitivity, its independence from inter-image comparisons,
402 and its versatility to imaging resolution and modality. While time-intensive conventional image
403 analyses and training-intensive machine learning approaches can only achieve sensitivity above 80%
404 with low specificity, our rapid automated method achieves 86% specificity with 81% sensitivity which
405 reduces radiologist burden in assessing algorithm false-positives. This computational tool can serve as
406 a second set of eyes to aid radiologist interpretation during UIA screening and has future value in
407 morphometry-based rupture risk prediction.

408
409 All algorithms herein described to process and display medical images for UIA detection are freely
410 available at <https://github.com/mcallenby/UIAdetection2020>.

411 Acknowledgements

412 Our algorithms use rapid anisotropic Euclidean distance transforms generated by Yuriy Mishchenko
413 (2015) and 3D medical image import algorithms by Dirk Jan Kroon (2011). We thank John Clouston
414 for fruitful discussions. This work is supported by a RBWH Foundation Grant to CW, MP, JC, MCA
415 and IHBI Inter-Theme Collaboration Grant to MCA and DAC. MCA is supported by an Advance
416 Queensland Fellowship.

417 Declaration of interests

418
419 The authors declare that they have no known competing financial interests or personal relationships that
420 could have appeared to influence the work reported in this paper.

421 CRediT author statement

422
423 **Mark C Allenby:** Conceptualization, methodology, software, formal analysis, validation, writing –
424 original draft, writing – review & editing, visualization, funding acquisition. **Ee Shern Liang:**
425 Resources, data curation, validation, writing – review & editing. **James Harvey:** Resources, data
426 curation, validation, writing – review & editing. **Maria A Woodruff:** Supervision, project
427 administration, writing – review & editing. **Marita Prior:** Resources, data curation, supervision, project
428 administration. **Craig Winter:** Resources, data curation, supervision, writing – review & editing,
429 funding acquisition. **David Alonso-Caneiro:** supervision, writing – review & editing, funding
430 acquisition.

431 References

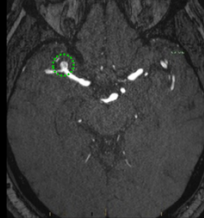
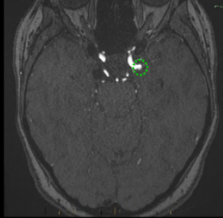
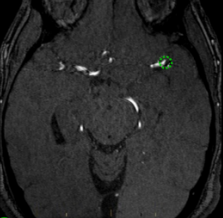
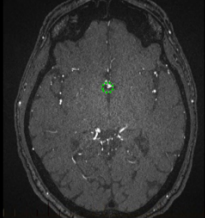
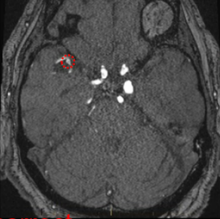
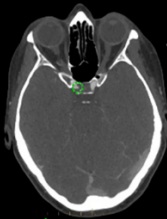
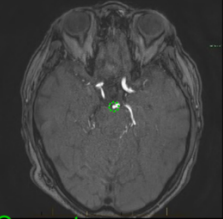
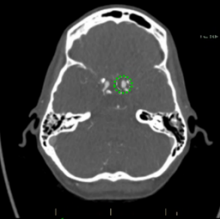
- 432
433 **References**
434 Bogunović, H., Pozo, J.M., Cárdenes, R., Villa-Uriol, M.C., Blanc, R., Piotin, M., Frangi, A.F., 2012.
435 Automated landmarking and geometric characterization of the carotid siphon. *Med. Image Anal.*
436 16, 889–903. <https://doi.org/10.1016/j.media.2012.01.006>
437 Chien, A., Callender, R.A., Yokota, H., Salamon, N., Colby, G.P., Wang, A.C., Szeder, V., Jahan, R.,
438 Tateshima, S., Villablanca, J., Duckwiler, G., Vinuela, F., Ye, Y., Hildebrandt, M.A.T., 2020.
439 Unruptured intracranial aneurysm growth trajectory: Occurrence and rate of enlargement in 520
440 longitudinally followed cases. *J. Neurosurg.* <https://doi.org/10.3171/2018.11.JNS181814>
441 Corfield, L., Speirs, A., McCormack, D.J., Waltham, M., 2010. Time of Flight Magnetic Resonance
442 Angiography: A Trap for the Unwary. *EJVES Extra* 19, e35–e37.
443 <https://doi.org/10.1016/j.ejvsextra.2010.01.002>
444 Duan, H., Huang, Y., Liu, L., Dai, H., Chen, L., Zhou, L., 2019. Automatic detection on intracranial
445 aneurysm from digital subtraction angiography with cascade convolutional neural networks.
446 *Biomed. Eng. Online* 1–18. <https://doi.org/10.1186/s12938-019-0726-2>
447 Duan, Z., Li, Y., Guan, S., Ma, C., Han, Y., Ren, X., Wei, L., Li, W., Lou, J., Yang, Z., 2018.
448 Morphological parameters and anatomical locations associated with rupture status of small
449 intracranial aneurysms. *Sci. Rep.* 8, 1–7. <https://doi.org/10.1038/s41598-018-24732-1>
450 Faron, A., Sijben, R., Teichert, N., Freiherr, J., Wiesmann, M., Sichtermann, T., 2019. Deep learning-
451 based detection of intracranial aneurysms in 3D TOF-MRA. *Am. J. Neuroradiol.* 40, 25–32.

- 452 <https://doi.org/10.3174/ajnr.A5911>
- 453 Forkert, N.D., Illies, T., Moller, D., H., H., Saring, D., Fiehler, J., 2012. Analysis of the Influence of
454 4D MR Angiography Temporal Resolution on Time-to-Peak Estimation Error for Different
455 Cerebral Vessel Structures. *Am. J. Neuroradiol.* 33, 2103–2109.
- 456 Huang, T.C., Chang, C.K., Liao, C.H., Ho, Y.J., 2013. Quantification of Blood Flow in Internal
457 Cerebral Artery by Optical Flow Method on Digital Subtraction Angiography in Comparison
458 with Time-Of-Flight Magnetic Resonance Angiography. *PLoS One* 8.
459 <https://doi.org/10.1371/journal.pone.0054678>
- 460 International Study of Unruptured Intracranial Aneurysms (ISUIA), 2003. Unruptured intracranial
461 aneurysms: natural history, clinical outcome, and risks of surgical and endovascular treatment.
462 *Lancet* 362, 103–110.
- 463 Ishibashi, T., Murayama, Y., Urashima, M., Saguchi, T., Ebara, M., Arakawa, H., Irie, K., Takao, H.,
464 Abe, T., 2009. Unruptured intracranial aneurysms: Incidence of rupture and risk factors. *Stroke*
465 40, 313–316. <https://doi.org/10.1161/STROKEAHA.108.521674>
- 466 Jan Kroon, D., 2011. Matlab File Exchange “Read Medical Data 3D” [WWW Document]. URL
467 <https://au.mathworks.com/matlabcentral/fileexchange/29344-read-medical-data-3d>
- 468 Jin, Z., Arimura, H., Kakeda, S., Yamashita, F., Sasaki, M., Korogi, Y., 2016. An ellipsoid convex
469 enhancement filter for detection of asymptomatic intracranial aneurysm candidates in CAD
470 frameworks. *Med. Phys.* 43, 951–960. <https://doi.org/10.1118/1.4940349>
- 471 Kerrien, E., Yureidini, A., Dequidt, J., Duriez, C., Anxionnat, R., Cotin, S., 2017. Blood vessel
472 modeling for interactive simulation of interventional neuroradiology procedures. *Med. Image*
473 *Anal.* 35, 685–698. <https://doi.org/10.1016/j.media.2016.10.003>
- 474 Leng, X., Wang, Y., Xu, J., Jiang, Y., Zhang, X., Xiang, J., 2018. Numerical simulation of
475 patient-specific endovascular stenting and coiling for intracranial aneurysm surgical planning. *J.*
476 *Transl. Med.* 16, 1–10.
- 477 Li, M.H., Cheng, Y.S., Li, Y.D., Fang, C., Chen, S.W., Wang, W., Hu, D.J., Xu, H.W., 2009. Large-
478 cohort comparison between three-dimensional time-of-flight magnetic resonance and rotational
479 digital subtraction angiographies in intracranial aneurysm detection. *Stroke.* 40, 3127–3129.
480 <https://doi.org/10.1161/STROKEAHA.109.553800>
- 481 Lin, A., Rawal, S., Agid, R., Mandell, D.M., 2018. Cerebrovascular Imaging: Which Test is Best?
482 *Clin. Neurosurg.* 83, 5–18. <https://doi.org/10.1093/neuros/nyx325>
- 483 Mair, G., 2015. Lack of flow on time-of-flight MR angiography does not always indicate occlusion.
484 *BJR|case reports* 2, 20150187. <https://doi.org/10.1259/bjrcr.20150187>
- 485 Mayo Foundation for Medical Education and Research, 2017. Patient Care & Helath Information:
486 Brain Aneurysm & Carotid Artery Disease [WWW Document]. URL
487 <https://www.mayoclinic.org/diseases-conditions/brain-aneurysm/diagnosis-treatment/drc-20361595>
488
- 489 Micieli, A., Kingston, W., 2019. An approach to identifying headache patients that require
490 neuroimaging. *Front. Public Heal.* <https://doi.org/10.3389/fpubh.2019.00052>
- 491 Miki, S., Hayashi, N., Masutani, Y., Nomura, Y., Yoshikawa, T., Hanaoka, S., Nemoto, M., Ohtomo,
492 K., 2016. Computer-assisted detection of cerebral aneurysms in MR angiography in a routine
493 image-reading environment: Effects on diagnosis by radiologists. *Am. J. Neuroradiol.* 37, 1038–
494 1043. <https://doi.org/10.3174/ajnr.A4671>
- 495 Mishchenko, Y., 2015. A fast algorithm for computation of discrete Euclidean distance transform in
496 three or more dimensions on vector processing architectures. *Signal, Image Video Process.* 9,
497 19–27. <https://doi.org/10.1007/s11760-012-0419-9>
- 498 Mouches, P., Forkert, N.D., 2019. A statistical atlas of cerebral arteries generated using multi-center
499 MRA datasets from healthy subjects. *Sci. Data* 6, 29. <https://doi.org/10.1038/s41597-019-0034-5>
- 500 Nakao, T., Hanaoka, S., Nomura, Y., Sato, I., Nemoto, M., Miki, S., Maeda, E., Yoshikawa, T.,
501 Hayashi, N., Abe, O., 2018. Deep neural network-based computer-assisted detection of cerebral
502 aneurysms in MR angiography. *J. Magn. Reson. Imaging* 47, 948–953.
503 <https://doi.org/10.1002/jmri.25842>
- 504 Nyúl, L.G., Udupa, J.K., Zhang, X., 2000. New variants of a method of MRI scale standardization.
505 *IEEE Trans. Med. Imaging.* <https://doi.org/10.1109/42.836373>
- 506 Okahara, M., Kiyosue, H., Yamashita, M., Nagatomi, H., Hata, H., Saginoya, T., Sagara, Y., Mori, H.,

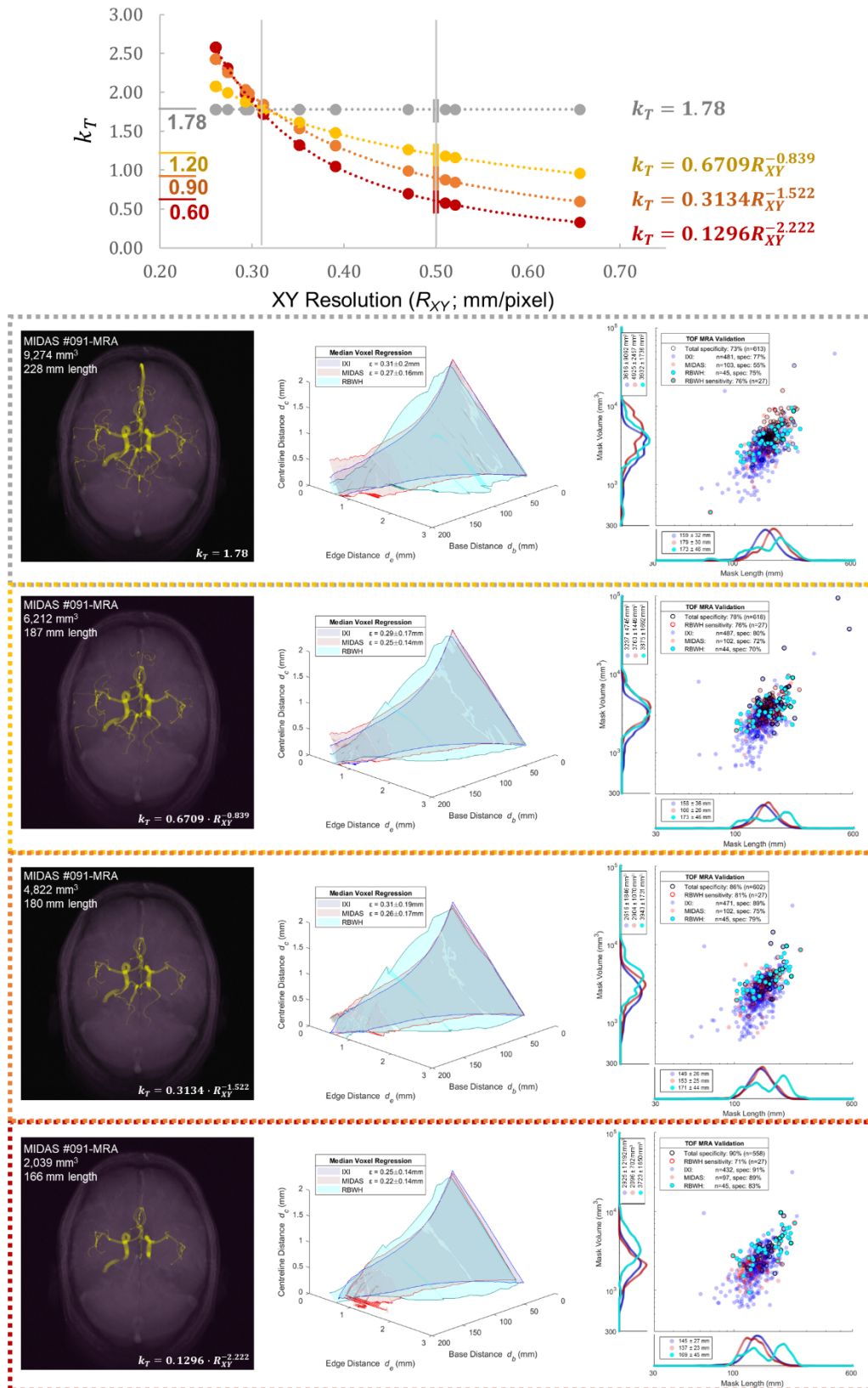
- 507 2002. Diagnostic accuracy of magnetic resonance angiography for cerebral aneurysms in
508 correlation with 3D-digital subtraction angiographic images: A study of 133 aneurysms. *Stroke*
509 33, 1803–1808. <https://doi.org/10.1161/01.STR.0000019510.32145.A9>
- 510 Pelka, O., Koitka, S., Johannes, R., Nensa, F., Friedrich, C.M., 2017. Intravascular Imaging and
511 Computer Assisted Stenting, and Large-Scale Annotation of Biomedical Data and Expert Label
512 Synthesis, MICCAI Workshop on Large-scale Annotation of Biomedical Data and Expert Label
513 Synthesis (LABELS). <https://doi.org/10.1007/978-3-319-67534-3>
- 514 Russell, J.H., Kelson, N., Barry, M., Percy, M., Fletcher, D.F., Winter, C.D., 2013. Computational
515 fluid dynamic analysis of intracranial aneurysmal bleb formation. *Neurosurgery* 73, 1061–1068.
- 516 Shi, Z., Hu, B., Schoepf, U.J., Savage, R.H., Dargis, D.M., Pan, C.W., Li, X.L., Ni, Q.Q., Lu, G.M.,
517 Zhang, L.J., 2020. Artificial Intelligence in the Management of Intracranial Aneurysms: Current
518 Status and Future Perspectives. *Am. J. Neuroradiol.* 41, 373–379.
519 <https://doi.org/10.3174/ajnr.A6468>
- 520 Shi, Z., Miao, C.C., Pan, C.W., Chai, X., Li, X.L., Xia, S., Gu, Y., Zhang, Y.G., Hu, B., Xu, W. Da,
521 Zhou, C.S., Luo, S., Wang, H., Mao, L., Liang, K.M., Yu, Y.Z., Lu, G.M., Zhang, L.J., 2020.
522 Clinically Applicable Deep Learning for Intracranial Aneurysm Detection in Computed
523 Tomography Angiography Images: A Comprehensive Multicohort Study. *medRxiv*
524 2020.03.21.20040063. <https://doi.org/10.1101/2020.03.21.20040063>
- 525 Stember, J.N., Chang, P., Stember, D.M., Liu, M., Grinband, J., Filippi, C.G., Meyers, P.,
526 Jambawalikar, S., 2019. Convolutional Neural Networks for the Detection and Measurement of
527 Cerebral Aneurysms on Magnetic Resonance Angiography. *J. Digit. Imaging* 32, 808–815.
528 <https://doi.org/10.1007/s10278-018-0162-z>
- 529 Štěpán-Buksakowska, I.L., Accurso, J.M., Diehn, F.E., Huston, J., Kaufmann, T.J., Luetmer, P.H.,
530 Wood, C.P., Yang, X., Blezek, D.J., Carter, R., Hagen, C., Hořínek, D., Hejčl, A., Růček, M.,
531 Erickson, B.J., 2014. Computer-aided diagnosis improves detection of small intracranial
532 aneurysms on MRA in a clinical setting. *Am. J. Neuroradiol.* 35, 1897–1902.
533 <https://doi.org/10.3174/ajnr.A3996>
- 534 Thompson, B.G., Brown, R.D., Amin-hanjani, S., Broderick, J.P., Cockroft, K.M., Connolly, E.S.,
535 Duckwiler, G.R., Harris, C.C., Howard, V.J., Johnston, S.C.C., Meyers, P.M., Molyneux, A.,
536 Ogilvy, C.S., 2015. AHA / ASA Guideline Guidelines for the Management of Patients With
537 Unruptured Intracranial Aneurysms. *Stroke* 46, 2368–2400.
538 <https://doi.org/10.1161/STR.0000000000000070>
- 539 Ueda, D., Yamamoto, A., Nishimori, M., Shimono, T., Doishita, S., Shimazaki, A., Katayama, Y.,
540 Fukumoto, S., Choppin, A., Shimahara, Y., Miki, Y., 2019. Deep learning for MR angiography:
541 Automated detection of cerebral aneurysms. *Radiology* 290, 187–194.
542 <https://doi.org/10.1148/radiol.2018180901>
- 543 van Gijn, J., Kerr, R.S., Rinkel, G.J., 2007. Subarachnoid haemorrhage. *Lancet* 369, 306–318.
544 [https://doi.org/10.1016/S0140-6736\(07\)60153-6](https://doi.org/10.1016/S0140-6736(07)60153-6)
- 545 Williams, L.N., Brown, R.D., 2013. Management of Unruptured Intracranial Aneurysms, in:
546 *Neurology: Clinical Practice*. pp. 99–108.
- 547 Wong, W.C.K., Chung, A.C.S., 2007. Probabilistic vessel axis tracing and its application to vessel
548 segmentation with stream surfaces and minimum cost paths. *Med. Image Anal.* 11, 567–587.
549 <https://doi.org/10.1016/j.media.2007.05.003>
- 550 Yang, X., Blezek, D.J., Cheng, L.T.E., Ryan, W.J., Kallmes, D.F., Erickson, B.J., 2011. Computer-
551 aided detection of intracranial aneurysms in MR angiography. *J. Digit. Imaging* 24, 86–95.
552 <https://doi.org/10.1007/s10278-009-9254-0>
- 553 Yang, X., Xia, D., Kin, T., Igarashi, T., 2020. IntraA: 3D Intracranial Aneurysm Dataset for Deep
554 Learning, arXiv.
555

556 **Supplemental Material**

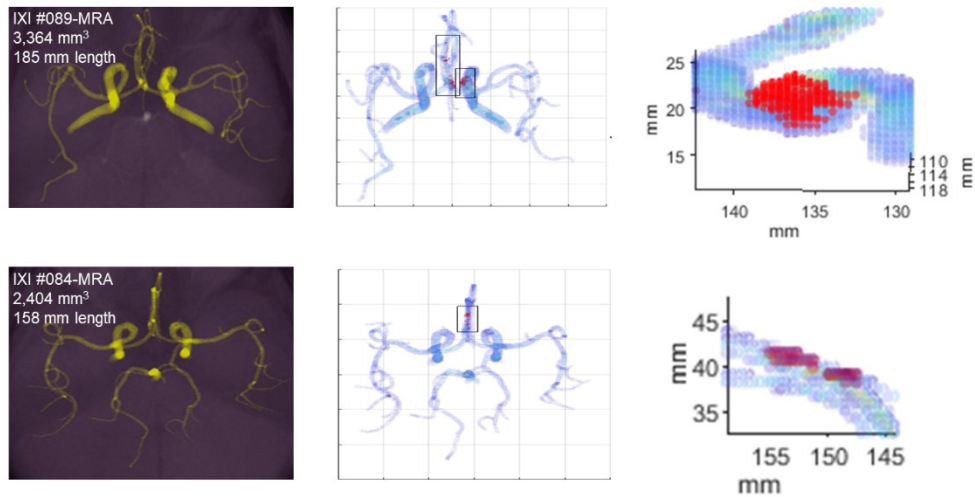
#	ANEURYSM LOCATION	MOST RECENT DIMENSIONS (AP x TR x CC) or maximal dimension	#	ANEURYSM LOCATION	MOST RECENT DIMENSIONS (AP x TR x CC) or maximal dimension
1	L MCA	3.5 mm	12	R ICA terminus	5.8 x 6 x 5.7 mm
2	R MCA	5 x 5 x 5 mm	13	L ICA terminus	3.4 x 4.3 x 3.6 mm
3	L PComA	4 x 3 mm	14	R ICA terminus	21 x 22 x 24 mm
4	L MCA	2 mm	15	Ophthalmic L ICA	6 x 4 x 4 mm
5	AComA	3.5 mm	16	Terminal L ICA	5 x 6 x 7 mm
6	AComA	4 x 5 x 3 mm	17	Basilar tip	2 x 2 x 2 mm
7	AComA	5 x 5 x 4.5 mm	18	L anterior pericallosal	1 mm
8	R MCA	3 mm	19	AcomA	6.3 x 7.7 x 6 mm
9	AComA	2 mm	20	Basilar/SCA origin	3 x 3 x 2.5 mm
10	L supraclinoid ICA	8.5 x 5 x 5.5 mm	21	R ICA (para-ophthalmic)	8 x 8 x 11 mm
11	R supraclinoid ICA	3 x 3 x 2.5 mm	22	L ICA terminus	7 x 5 x 3.5 mm

<p>UIA #2: R MCA</p>  <p>Correct</p>	<p>UIA #3: L PcomA</p>  <p>Correct</p>	<p>UIA #4: L MCA</p>  <p>Correct</p>	<p>UIA #5: AComA</p>  <p>Correct</p>
<p>UIA #8: R MCA</p>  <p>Incorrect</p>	<p>UIA #11: R supra ICA</p>  <p>Correct</p>	<p>UIA #20: Basilar/SCA</p>  <p>Correct</p>	<p>UIA #22: L ICA term</p>  <p>Correct</p>

557 **Figure S1: Radiologist-identified RBWH UIA sizes and locations.** (top) De-identified table of
 558 representative UIA locations and measured dimensions where number corresponds to (bottom)
 559 radiologist annotated MRA or CTA images and the ability of our computational approach to correctly
 560 or incorrectly detect UIAs. Annotations include: L/R, left/right; MCA, middle carotid artery; PComA,
 561 peripheral communicating artery; AComA, anterior communicating artery; ICA, internal carotid artery;
 562 SCA, subclavian artery; AP, anteroposterior measurement; TR, traverse measurement; CC,
 563 craniocaudal (coronal) measurement.



564 **Figure S2: Impact of k_T normalisation on R_{XY} during validation and assessment.** The constant $k_T =$
 565 1.78 appeared ideal for images with XY resolution of $R_{XY} = 0.32$ mm/voxel but incorrectly segmented
 566 images with poorer R_{XY} near 0.5 mm/voxel. Power regressions are compared which normalise k_T values
 567 to 1.2 (yellow), 0.9 (orange), and 0.6 (red) at a R_{XY} of 0.5 mm/voxel while maintaining $k_T = 1.78$ at R_{XY}
 568 = 0.32 mm/voxel. Linear regressions at similar intercepts were also compared with poorer low R_{XY}
 569 image segmentations. Columns 2 and 3 of the grey and orange boxes are displayed in Figure 5.



570 **Figure S3:** Examples of false-positive identifications in the carotid siphon (80% of false-positives; top
571 row) and anterior cerebral artery (20% of false positives; bottom row) for poor resolution IXI repository
572 TOF MRA images (0.47 x 0.47 x 0.8 mm/voxel). The carotid siphon anatomy rapidly changes diameter
573 and angle in different ways for different patients, which produces false-positive detections of dissecting
574 aneurysms (top right). The poor resolution images segment anterior cerebral arteries that comprise only
575 a few voxels in diameter, and due to their low resolution, these arteries appear to overlap during
576 segmentation, creating false-positive artefacts.